nature photonics

ARTICLES

PUBLISHED ONLINE: 17 APRIL 2017 | DOI: 10.1038/NPHOTON.2017.43

Monolithic integration of hybrid perovskite single crystals with heterogenous substrate for highly sensitive X-ray imaging

Wei Wei[1†], Yang Zhang[1†], Qiang Xu[2], Haotong Wei[1], Yanjun Fang[1], Qi Wang[1], Yehao Deng[1], Tao Li[3], Alexei Gruverman[3], Lei Cao[2] and Jinsong Huang[1*]

The monolithic integration of new optoelectronic materials with well-established inexpensive silicon circuitry is leading to new applications, functionality and simple readouts. Here, we show that single crystals of hybrid perovskites can be integrated onto virtually any substrates, including silicon wafers, through facile, low-temperature, solution-processed molecular bonding. The brominated (3-aminopropyl)triethoxysilane molecule binds the native oxide of silicon and participates in the perovskite crystal with its ammonium bromide group, yielding a solid mechanical and electrical connection. The dipole of the bonding molecule reduces device noise while retaining signal intensity. The reduction of dark current enables the detectors to be operated at increased bias, resulting in a sensitivity of 2.1×10^4 μC Gy_{air}^{-1} cm^{-2} under 8 keV X-ray radiation, which is over a thousand times higher than the sensitivity of amorphous selenium detectors. X-ray imaging with both perovskite pixel detectors and linear array detectors reduces the total dose by 15–120-fold compared with state-of-the-art X-ray imaging systems.

X-ray detectors are widely applied in medical imaging, the non-destructive inspection of luggage and industrial products, and scientific research[1–5]. Solid-state semiconductor detectors, which directly convert X-ray photons to an electrical signal, are attractive for these applications due to their simplicity, compactness, robustness and capability to form detector arrays for imaging[2–4]. High detection efficiency, high sensitivity and large peak-to-background ratio are generally regarded as the most important figures of merit for X-ray detectors in order to reduce the X-ray dose to which patients are exposed during medical check-ups and to detect weaker X-ray signals, and these factors are closely related to the charge carrier mobility and lifetime ($\mu\tau$) product as well as the atomic number Z of the semiconductor materials. With the rapid advances in semiconductor fabrication already achieved, various materials have been exploited for use in X-ray detectors. Most are crystalline materials, such as silicon, germanium and cadmium zinc telluride, among others[5–7]. However, amorphous selenium (α-Se), despite its small Z and $\mu\tau$, has dominated the medical X-ray imaging market because it can be deposited at low temperatures onto Si thin-film transistor (TFT) arrays—which are mature technologies—to be read out in large flat panels[2,8].

Very recently, organic–inorganic hybrid perovskites (OIHPs), which have been shown to be excellent optoelectronic materials for solar cells[9–18], photodetectors[19], light-emitting diodes[20] and lasers[20], joined the family of semiconductors used for X-ray detectors, as a very promising candidate[11,21]. These materials combine many of the preferred intrinsic properties for X-ray detection, including a large proper bandgap (E_g) of 1.6–3.0 eV (refs 9, 16) to reduce thermal noise, a large $\mu\tau$ product on the order of ~10^{-2} cm^2 V^{-1} due to the small electron effective mass and extremely low trap density[21–23], the high-Z element Pb in the compound, and a large density of 4.5 g cm^{-3}. In addition to its good performance for X-ray detection, as demonstrated recently[21,22], the simple low-temperature synthesis of its single crystals give rise to the possibility of forming a large-area flat-panel detector array at low cost. Notably, $MAPbBr_3$ single crystals can be synthesized in solution at low temperatures[9,15,16], which is compatible with Si technology, and without damaging the substrate. This kind of integration would be attractive in achieving high-sensitivity X-ray detectors, providing a feasible way to meet the application requirements for medical imaging by combining the crystals with thin-film transistors to form active-matrix flat-panel imagers.

In this Article, we report a simple technique to monolithically integrate $MAPbBr_3$ single crystals onto Si substrates so that the electric signal can be directly read out from Si. An NH_3Br-terminated molecule layer is used to mechanically and electrically connect the $MAPbBr_3$ single crystals with the Si, without any requirements for lattice matching with the Si substrates. The Si-integrated $MAPbBr_3$ single crystal devices demonstrate over 1,000 times better sensitivity than α-Se detectors to X-rays, and are able to image with a 15–120-fold weaker dose to the patient.

The mechanical adhesion of $MAPbBr_3$ single crystals to Si wafers is very weak if the single crystals are grown directly on the Si because of the weak bonds between them (hydrogen bonds and van der Waals interactions). To address this we added a layer of brominated (3-aminopropyl) triethoxysilane (APTES; chemical structure shown in Fig. 1a) to connect the perovskite and Si through primary chemical bonds. Figure 1a provides a schematic of the low-temperature, solution-processed, molecular bonding procedure for a Si-integrated $MAPbBr_3$ single crystal. Highly reactive Si–OH groups are generated by the hydrolysis of $Si–O–C_2H_5$ groups on an APTES molecule, which can bond with the –OH on the Si wafer via a condensation process to form strong covalent Si–O–Si bonds[24] and obtain NH_2-terminated molecular layers on the Si wafer. The

[1]Department of Mechanical and Materials Engineering, University of Nebraska-Lincoln, Lincoln, Nebraska 68588, USA. [2]Nuclear Engineering Program, Department of Mechanical and Aerospace Engineering, The Ohio State University, Columbus, Ohio 43210, USA. [3]Department of Physics and Astronomy, University of Nebraska-Lincoln, Lincoln, Nebraska 68588-0299, USA. †These authors contributed equally to this work. *e-mail: jhuang2@unl.edu

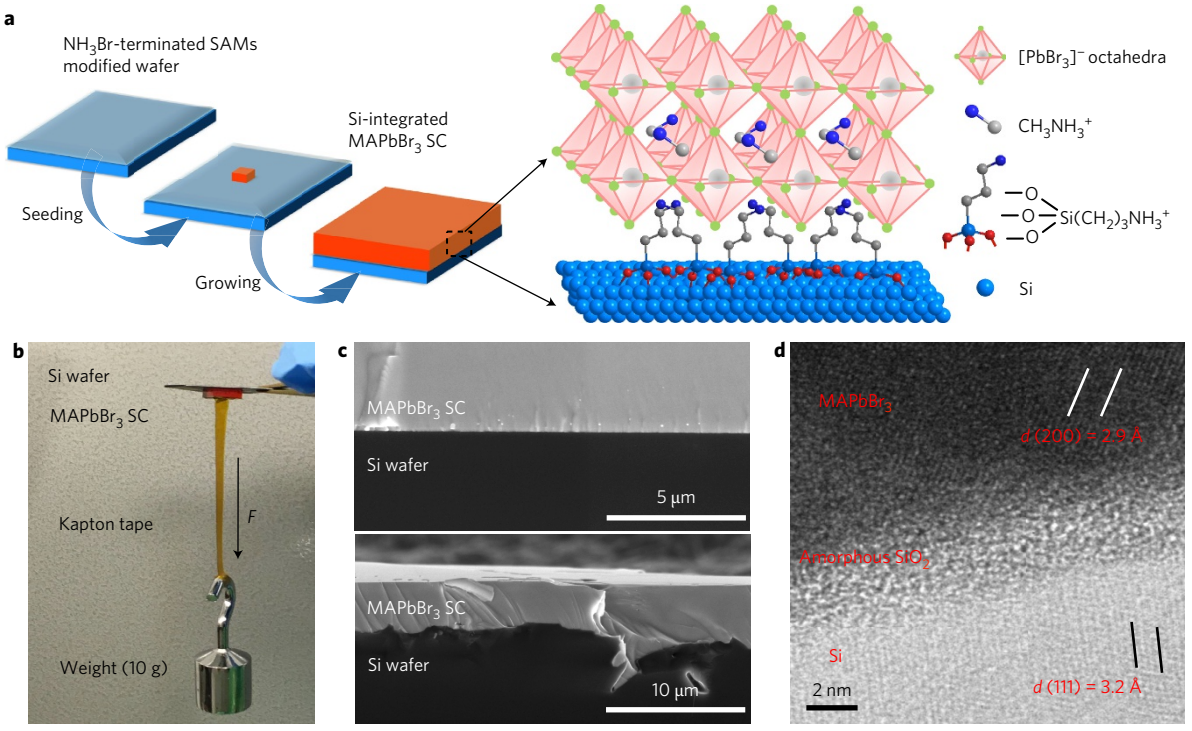

Figure 1 | Structure and morphology of the Si-integrated $MAPbBr_3$ single crystals. a, Schematic illustration of the fabrication of Si-integrated $MAPbBr_3$ single crystals (SCs) (not to scale—the silane thickness is highly exaggerated for clarity). **b**, Photograph of Si-integrated $MAPbBr_3$ single crystal with a 10 g weight attached to the $MAPbBr_3$ crystal by Kapton tape. **c**, SEM images of the cross-section of a $MAPbBr_3$ single crystal grown on a flat Si wafer (top) and rough Si wafer (bottom). **d**, High-resolution TEM image of the cross-section of the interface of the Si-integrated $MAPbBr_3$ single crystal, with the Si lattice and $MAPbBr_3$ lattice labelled.

basic $-NH_2$ groups can react with hydrobromide to form the $-NH_3Br$ salt, which participates in the formation of perovskite by reacting with the $PbBr_2$. The $[-Si(CH_2)_3NH_3]^+$ binds to $[PbBr_3]^-$ on the surface of a $MAPbBr_3$ single crystal close to the Si wafer[25], as shown in Fig. 1a. The brominated APTES layer performs as a bridge so that it naturally bonds Si with $MAPbBr_3$ crystals. We applied the modified reverse-solubility method to grow $MAPbBr_3$ single crystals on a Si wafer[15]. A pre-seeded $MAPbBr_3$ single crystal with dimensions of <300 μm was placed onto the wafer, modified with NH_3Br-terminated molecules, and grown to a thickness of 2–3 mm (sufficient to absorb most of the X-ray energy below 50 keV) by immersing the Si wafer in $MAPbBr_3$/DMF solution at 70 °C for 6–8 h.

As a result of the chemical bonds formed at the interface, the single crystals grown on the functionalized Si wafers had a solid mechanical and electrical connection between the Si and the perovskite crystals. Figure 1b shows a $MAPbBr_3$ single crystal with an area of 5.8 mm × 5.8 mm, integrated onto the Si wafer, which can bear its own gravity plus an added weight of 10 g, which corresponds to a tensile pressure of 3.5 kPa. We also demonstrated that the perovskite crystals could be grown on rough Si wafers formed by scratching them with sandpaper. The cross-sectional scanning electron microscope (SEM) images in Fig. 1c show the interfacial morphology of the $MAPbBr_3$ single crystal growing on flat and sandpaper-scratched Si wafers, which reveals successful integration of $MAPbBr_3$ with Si in both cases. For the $MAPbBr_3$ grown on a rough Si wafer, the single crystals closely fit with the substrates with the same orientation (Supplementary Fig. 1), increasing the contact area between the wafer and single crystal and thus resulting in better mechanical adhesion of the $MAPbBr_3$ single crystals and Si wafers without compromising the electric properties, as shown in the following. The high-resolution transmission electron microscopy (TEM) image in Fig. 1d of the Si–$MAPbBr_3$ interface reveals a 2- to 3-nm-thick amorphous region between the crystalline lattices of Si and $MAPbBr_3$, which can be assigned to be native SiO_2, a brominated APTES molecule layer (~1 nm thick) in between, and some amorphous $MAPbBr_3$ close to the $MAPbBr_3$ single crystal side.

An interesting finding is the automatic transition of $MAPbBr_3$ material growth from the amorphous to crystalline phases, despite the absence of a lattice match between Si and $MAPbBr_3$. This can be explained by the soft nature of hybrid perovskites, which enables a quick transition from the amorphous to crystal phase at the interface, with small critical thickness. Young's modulus of the hybrid perovskite is at least one order of magnitude smaller than those of most regular inorganic semiconductors, such as GaN, Si and GaAs (refs 26–31). It requires lower energy to create a dislocation to relax the lattice mismatch strain, so the strain can be accommodated by a thinner epitaxial layer of lattice-mismatched material with a critical thickness of ~1–3 nm. The results indicate that the perovskite crystals can be grown virtually on any substrate that can bond to APTES molecules. To verify this, we also grew $MAPbBr_3$ single crystals on the many surfaces that are needed for different types of device integration, such as indium tin oxide (ITO) or other types of oxides, metals and even glass, as shown in Supplementary Fig. 2. Although the perfect lattice-matched system of perovskite–lead sulfide quantum dots (PbS QDs) was shown to passivate the PbS QDs and enhance their optoelectronic properties[32], the relief of the lattice matching constraint enables the integration of perovskite materials heterogeneously with many other electronic and optical materials and substrates, thus opening up much broader fields for the application of perovskite materials.

The device structure, shown in Fig. 2a, was constructed to characterize the electronic properties of the Si/$MAPbBr_3$ interface. Layers of C_{60} (20 nm), bathocuproine (BCP) (8 nm) and Au (25 nm) were sequentially deposited on the $MAPbBr_3$ single crystals on

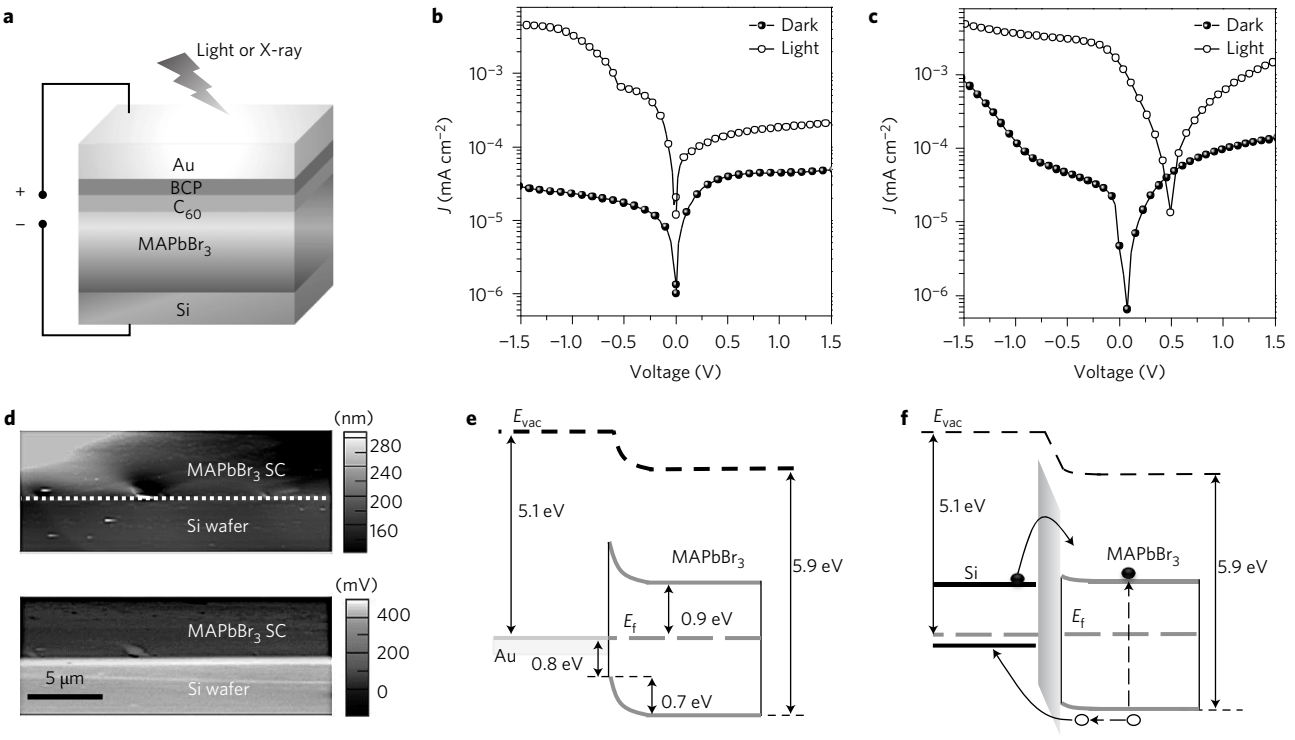

Figure 2 | Properties of the interfacial connection in the Si-integrated $MAPbBr_3$ single crystal device. a, Schematic illustration of the structure of Si-integrated $MAPbBr_3$ single crystal devices. **b**,**c**, Dark current and photocurrent density of the Si-integrated $MAPbBr_3$ single crystal device (**b**) and the Au-anode $MAPbBr_3$ single crystal device (**c**, control device). The thickness of the $MAPbBr_3$ single crystals used in **b** and **c** was ~2.0 mm, and the light intensity, ~2×10^{-4} W cm^{-2}, was the same for the two devices. **d**, Height image (top) and KPFM image (bottom) of a cross-section of the Si-integrated $MAPbBr_3$ single crystal. **e**, Energy level diagram for the interface of the Au/$MAPbBr_3$ single crystal. **f**, Energy level diagram for the interface of the Si/$MAPbBr_3$ single crystal with the dipole layer.

the side opposite the Si, to act as a cathode, with Si working as the anode. Light entered through the translucent Au. The device structure was eventually the same as the previously created structure[21], but with the anode electrode now comprising highly doped Si and replacing the Au for charge readout. For comparison, we also fabricated devices with Au as the anode by following previous procedures[21] and used them as control devices (termed Au/$MAPbBr_3$ single crystal devices hereafter). A substantial difference in optoelectronic properties was observed. The absence of a notable photovoltage for the device under illumination (Fig. 2b) indicated that the Si/$MAPbBr_3$ contact is not a Schottky junction, although the different materials and interfacial dipoles may still cause rectification, as also shown in Fig. 2b. This is in strong contrast to the Schottky junction formed by Au/$MAPbBr_3$ contacts. To understand the interface energy levels, we used Kelvin probe force microscopy (KPFM) to scan the potential profile of the cross-section of the Si/$MAPbBr_3$ interface. As shown in Fig. 2d, there was an abrupt potential change at the Si/$MAPbBr_3$ interface of 0.5–0.6 eV. We speculate it was caused by the dipole of the brominated APTES molecule. To verify this, we measured the surface potential of bare Si and NH_3Br-terminated molecule-covered Si and observed the same workfunction shift (Supplementary Fig. 3). We can thus sketch the energy diagram at the Au/$MAPbBr_3$ and Si/$MAPbBr_3$ interfaces based on the reported energy levels of $MAPbBr_3$ (ref. 10). As shown in Fig. 2e, a Schottky junction was formed at the Au/$MAPbBr_3$ interface with a band bending of 0.7 eV to align the Fermi levels of Au and $MAPbBr_3$, while the shift of the vacuum level by the brominated APTES dipoles aligned the Fermi levels of Si and $MAPbBr_3$ and thus resulted in the formation of the rectification-less contact.

The dipole layer, with a large energy barrier for electron injection but small energy barrier for hole extraction, yielded a small dark current and a large photocurrent in the Si-integrated $MAPbBr_3$ single crystal device. The dark current density J_d was 3–30 times lower than the Au/$MAPbBr_3$ single crystal device under the same reverse bias (Fig. 2b,c), with a stronger dark current suppression at higher bias. The J_d of 23 nA cm^{-2} at −1 V bias of the Si-integrated device was even smaller than that of the control device at −0.1 V bias. This allowed the operation of the devices as light and X-ray detectors at a much higher bias to enhance signal output and for a quicker response speed. The inserted dipole layer did not sacrifice the photocurrent. The Si-integrated $MAPbBr_3$ single crystal device had the same value of photocurrent as the control device under −1 V bias.

The small dark current and large photocurrent of the Si-integrated device enabled sensitive light and X-ray detection. We first evaluated the visible light detection properties of the Si-integrated $MAPbBr_3$ single crystal devices. The external quantum efficiency (EQE) measurement, shown in Fig. 3a, shows that the Si-integrated $MAPbBr_3$ single crystal device has 70% average internal quantum efficiency (IQE) with a maximum value around 90% under −1 V bias. The close-to-unity IQE indicates a nearly 100% charge collection efficiency of the Si-integrated $MAPbBr_3$ single crystal device, which is about a twofold improvement over the Au/$MAPbBr_3$ device[21]. Figure 3b shows the photocurrent responses of the Si-integrated $MAPbBr_3$ single crystal device and the control device under irradiance from a 390 nm LED. The responsivity R of the Si-integrated device at −1 V bias was also two times higher than that of the control device, agreeing with the doubled IQE of the Si-integrated device. The Si-integrated $MAPbBr_3$ device showed a low noise current of 0.05 pA Hz$^{-1/2}$ under −1 V bias at 35 Hz (Supplementary Fig. 4a); this was independent of frequency and close to the calculated shot noise limit from the dark current

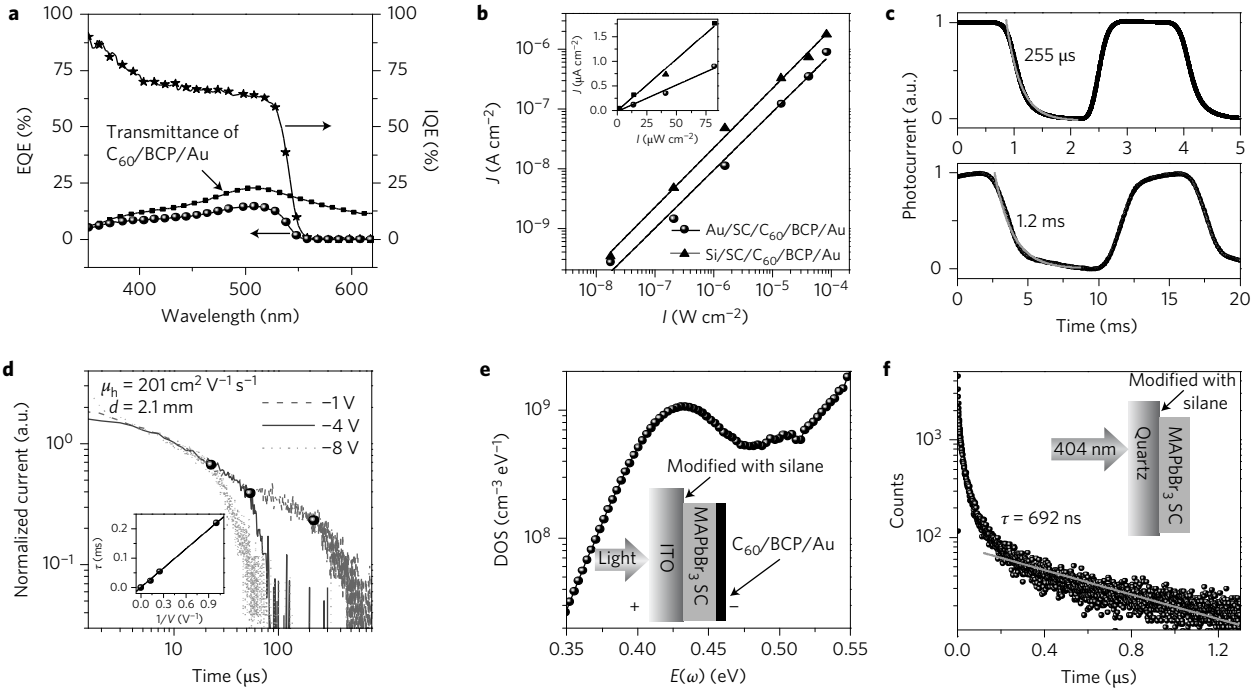

Figure 3 | Superior photodetection performance of the Si-integrated $MAPbBr_3$ single crystal device. The thickness of the $MAPbBr_3$ single crystal is ~2.0 mm. **a**, EQE and IQE of the Si-integrated $MAPbBr_3$ single crystal devices at –1.0 V bias. **b**, Photocurrent density versus light intensity for the Si-integrated $MAPbBr_3$ single crystal device under –1.0 V bias and the Au/$MAPbBr_3$ single crystal device (control device) at –0.1 V bias. **c**, Temporal response of the Si-integrated $MAPbBr_3$ single crystal device at –1.0 V bias (top) and control device at –0.1 V bias (bottom). **d**, Normalized transient current curves of the Si-integrated $MAPbBr_3$ single crystal device under various biases. Inset: charge transit time versus reciprocal of the bias. The solid line is a linear fit to the data. **e**, Trap density of states (t-DOS) of the $MAPbBr_3$ single crystal integrated on ITO glass modified with NH_3Br-terminated molecules. **f**, Photoluminescence surface recombination lifetime of the $MAPbBr_3$ single crystal growing on quartz modified with NH_3Br-terminated molecules.

(Supplementary Fig. 4b). To maintain the low noise, we operated the devices at −1 V for light detection. A maximum specific detectivity D^* of 2×10^{12} cm $Hz^{1/2}$ W^{-1} was derived from the IQE and the noise current (Supplementary Fig. 4c). The response time in Fig. 3c was derived from the decay process of the photocurrent curve measured with a chopper under a low excitation intensity of several microwatts per square centimetre (μW cm^{-2}). The Si-integrated device showed a rapid response time of 255 μs under −1 V bias, which is five times faster than that of the control device under −0.1 V bias. The less than 10 times enhancement can be explained by the existence of a built-in field in the control device. The transport properties of $MAPbBr_3$ single crystals grown on Si were essentially the same as those grown in solution, as evidenced by the same carrier mobility of 201 cm^2 V^{-1} s^{-1} measured by time of flight (ToF) (Fig. 3d). The mobility–lifetime ($\mu\tau$) product of the $MAPbBr_3$ single crystal was comparable to those best grown in solution without Si integration, as confirmed by the steady-state photoconductivity measurement shown in Supplementary Fig. 5. We note that the $\mu\tau$ extracted from the steady-state photoconductivity measurement may be different from values obtained from other measurements, such as the direct measurement of carrier recombination lifetime by photoluminescence decay[19]. Nevertheless, the photoconductivity method has been commonly applied to extract values of $\mu\tau$ for the assessment of X-ray detection materials in the community[7,33,34], which facilitates a comparison of the candidate materials for X-ray detection. To study the optoelectronic property of the interfacial connection layer, we integrated the $MAPbBr_3$ single crystal onto ITO glass so that light could come directly to this interfacial layer through the transparent ITO glass, as shown in Fig. 3e. The trap density of the crystal close to the ITO (modified with NH_3Br-terminated molecules), as measured by impedance spectroscopy, showed a value of 10^8–10^9 cm^{-3} eV^{-1}, comparable with that of the Au/$MAPbBr_3$ single crystal device[21]. The surface charge recombination rate was exploited by a photoluminescence lifetime measurement of a quartz-integrated $MAPbBr_3$ single crystal. Light from the incident laser (404 nm) penetrated the quartz without attenuation and was absorbed by the very thin surface layer of the crystal close to the brominated APTES molecular layer, due to the small penetration length of 180 nm for 404 nm light in $MAPbBr_3$. The measured charge recombination lifetime should represent the charge recombination process at the surface, combined with the diffusion of carriers away from the crystal surface[11]. A long lifetime of 692 ns was derived from the fitting curve in Fig. 3f, which is comparable to the values measured from other facets of the same crystals without surface passivation. This comparable trap density, as well as the charge recombination lifetime, indicates that the very thin amorphous perovskite layer at the silicon/perovskite interface did not cause additional trap states or additional charge quenching sites, which can be explained by the unique defect-tolerant nature of the hybrid perovskite predicted by theory[35].

Due to the excellent charge collection efficiency and strong stopping power of the $MAPbBr_3$ single crystals, the Si-integrated $MAPbBr_3$ single crystal device showed a sensitive response to X-rays. We fabricated 2.0-mm-thick Si-integrated $MAPbBr_3$ devices to investigate them under X-rays with an energy of 50 keV, and we also fabricated thinner (~150 μm) devices to test their imaging capabilities, because the X-ray imaging system we used is limited by an X-ray source with a peak energy of ~8 keV. The 2.0-mm-thick Si-integrated $MAPbBr_3$ devices showed a clear response to X-rays on turning the incident X-ray on and off, as shown in Supplementary Fig. 6. To evaluate the sensitivity and lowest detectable dose rate of the Si-integrated $MAPbBr_3$ single crystal detectors, we controlled the total X-ray dose by changing the current of the X-ray tube or adding multiple-layer Al foil as a filter, with the

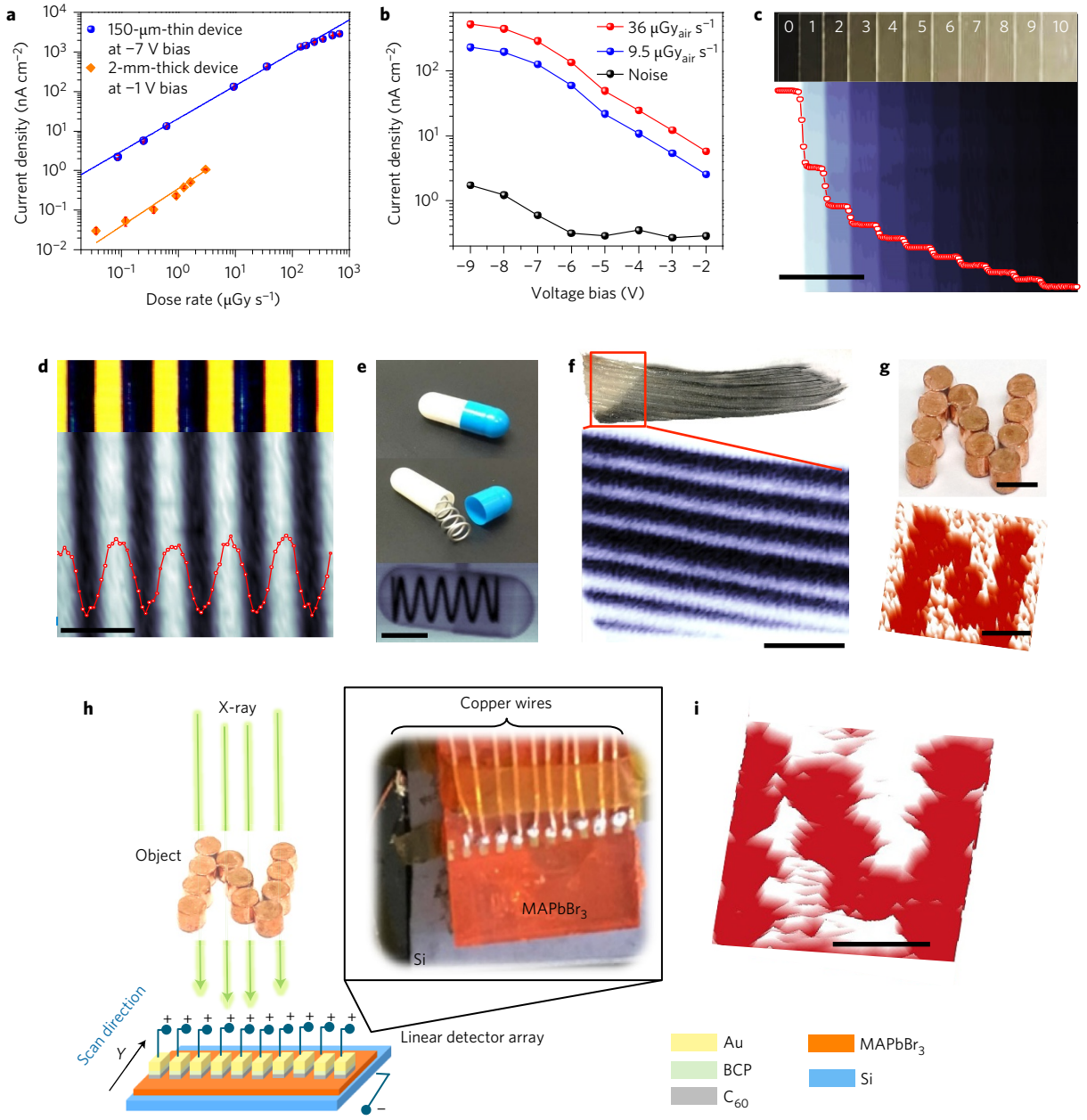

Figure 4 | X-ray detection and imaging performance. **a**, X-ray-generated photocurrent versus dose rate. **b**, X-ray-induced current density of a 150-μm-thin crystal device under different X-ray intensities. This device was used for the X-ray imaging in **c**–**g**. **c**, Optical (top) and X-ray (bottom) images of stacked glass coverslips. **d**, Optical image (top) of a stainless-steel plate with etched-through lines and its X-ray image with current profile (bottom). **e**, Optical and X-ray images of an encapsulated metallic spring. **f**, Optical image of a portion of a fish caudal fin (top) and X-ray image of a section of it (bottom). **g**, Photo (top) and X-ray image (bottom) of an 'N' copper logo under a dose rate of 247 nGy_{air} s^{-1}. **h**, Schematic illustration of X-ray imaging with Si-integrated $MAPbBr_3$ single crystal detectors. **i**, X-ray image of the N-shaped logo obtained by the linear detector array. Scale bars: 200 μm (**d**) and 5 mm (**c**,**e**,**f**,**g**,**i**).

detection geometry shown in Supplementary Fig. 7; the device current densities at different dose rates are shown in Fig. 4a. The sensitivity of the detector was derived from the slope of the device output current density versus X-ray dose rate. A dramatically enhanced sensitivity of 322 μC Gy_{air}^{-1} cm^{-2} at −1 V bias was obtained for the 2.0-mm-thick device under 50 keV X-rays, which is four times higher than the sensitivity achieved with the control device of the same size[36]. The enhanced sensitivity can be explained by the twofold enhancement of charge collection efficiency and the larger bias applied compared with previous detectors, which again highlights the significance of the reduced noise current of the detectors. The low noise current of the Si-integrated devices also gave rise to a reduction in the lowest detectable X-ray dose rate, and thus improved the sensitivity to a weaker X-ray dose. The current signal generated from the device by the X-rays with a dose rate of 0.036 $μGy_{air}$ s^{-1} was easily distinguished from the noise, with good fidelity, representing a 14-fold improvement over what was obtained previously[21]. Eventually, the theoretical lowest detectable X-ray dose could be reached by further reducing the dark current to the level where quantum noise dominated, at which point one can use the concept of detection limits by merely measuring the background radiation to deduce the lowest detectable dose[37]. The signal and noise of a thinner device under a different bias and dose rate (8 keV X-ray) are shown in Fig. 4b. It can be seen that the signal intensity is tens to hundreds of times larger than the noise, even under a low dose rate of 9.5 $μGy_{air}$ s^{-1}. The signal-to-noise ratio

reached its peak at a bias of −7 V, and we thus chose −7 V as the working bias for the subsequent sensitivity and imaging measurement. As shown in Fig. 4a, although a much larger applied field did not improve the low detection limit of the thinner device, it did increase the sensitivity by more than 64-fold compared with the thick devices, resulting in a giant sensitivity of 2.1×10^4 μC Gy_{air}^{-1} cm^{-2} under 8 keV X-rays. This is over 1,000-fold larger than that of α-Se X-ray detectors, which can be explained by the presence of photoconductive gain of >100 (from the ratio of the measured photocurrent and the calculated photocurrent without gain) in the devices and a several orders of magnitude larger $\mu\tau$ product than in α-Se. We speculate it is the charge carrier traps at the perovskite/silicon interface that induce the gain under high bias, because all other surfaces are already passivated by oxidization[20].

The imaging capability of the Si-integrated $MAPbBr_3$ detectors was characterized by moving the objects on an X–Y stage while collecting the electrical signal of the detector with its position fixed. The thinner detectors were prepared as small pixels with an area of 0.044 mm^2 for imaging purpose. We first performed an imaging contrast test. As shown in Fig. 4c, ten glass coverslips (each ~150 μm thick) were stacked and offset to act as X-ray attenuators. In the figure, the numbers indicate the layers and the circles plot the averaged photocurrent on a semi-logarithmic plot. The captured image shows a clear contrast between the different layers of coverslips; the thicker the stacks of coverslips, the darker the image. The very good contrast is made explicit by the well-defined staircase appearance of the current output. The distinct step near the lowest current demonstrates the detector's capability to discriminate a dose rate of ~11.8 μGy_{air} s^{-1}. To demonstrate the capability of the imaging system to resolve small features, a stainless-steel plate patterned with etched-through lines of width ~80 μm and spacing ~80 μm was scanned by a device with dimensions of 100 μm × 250 μm and with the long axis parallel to the slits (Fig. 4d). Distinct bright and dark stripes are displayed in the image, suggesting that the system is able to distinguish object feature sizes of ~80 μm or smaller, which satisfies most medical imaging requirements and is among the best reported results[22,38]. In addition, we attempted to estimate the modulation transfer function (MTF) of our system by applying a fast Fourier transform (FFT) to one of the current peaks in the profile shown in Fig. 4d. The resulting MTF is shown in Supplementary Fig. 8. The resolution is ~10 line pairs per millimetre (lp mm^{-1}) at 20% MTF value, which is more than two times larger than that of the most recently reported X-ray detectors (4.75 lp mm^{-1})[38]. We remark that, for single-pixel detectors, the spatial resolution of the X-ray imaging is mainly limited by the size of the pixel, the distance between the object and the detector, and the thickness of the crystal, although the applied electric field also has an effect on the contrast resolution of the X-ray imaging. For the ten pixel linear array detectors discussed in the following, the spatial resolution is not only limited by the pixel size but also by the spacing (pitch) between the pixels. The unique capability of using X-rays for imaging is seeing through substances that are otherwise opaque to visible light. We concealed a metallic spring in an opaque capsule and imaged the closed capsule with X-rays (Fig. 4e). Due to the large difference in X-ray stopping, the spring inside the capsule is clearly revealed by the contrast apparent in the radiograph. In addition, one can even discern the wall thickness difference of the capsule in the overlapping region of the white and blue parts of the capsule. To simulate the application of Si-integrated detectors in medical radiography, a section of a fish caudal fin was scanned and the recorded image is shown in the bottom panel of Fig. 4f. It is clear that the rays and membranes between are well resolved, as indicated by the sharp contrast in the image.

The direct integration of perovskite crystals onto Si wafer allowed us to fabricate an X-ray linear detector array that has a performance close to those of industrial-level products on the market and enables much quicker scanning. As shown by the photo in Fig. 4h (inset), ten pixel electrodes were deposited on the top surface of a Si-integrated $MAPbBr_3$ single crystal (thickness of 2 mm), arranged in a line with a pixel size of 200 μm and a pitch of 400 μm. The Si-integrated linear detector array thus provided a scanning width of ~4 mm. The pixels were connected by individual copper wires to the current amplifier, with the Si substrate acting as the common anode. Sensitive X-ray imaging with the perovskite linear detector array was demonstrated with the set-up illustrated in Fig. 4h. In brief, the attenuated X-rays were detected by the linear detector array after passing a copper 'N'-shaped logo (photo in Fig. 4g). The logo was moved linearly in one direction, and the electrical signal from the linear detector array was read by a home-built switching system that can switch the connection between the common current amplifier and the different pixels. To scan the logo (dimensions of ~10 mm), two scans were conducted and the images were merged to form a full image (Fig. 4i). To demonstrate the capability of the highly sensitive Si-integrated linear detector array for X-ray imaging at low doses, we scanned the 'N' logo under an extremely low X-ray dose rate of 247 nGy_{air} s^{-1}. The copper cylinders were well distinguished from one another in the obtained images (Fig. 4i). The image quality measured at the same dose rate is very close to that obtained from a single-pixel detector while scanning in both X and Y directions (Fig. 4g). In dose evaluation of X-ray imaging, the dose–area product (DAP) rate is a practical quantity used to compare absorbed doses[39,40]. We estimate the DAP rate for capturing an image (entrance area of 100 cm^2) of the human body with a Si-integrated perovskite detector array (Supplementary Fig. 7). Assuming the lowest X-ray dose rate of 247 nGy_{air} s^{-1}, after penetrating the 20-cm-thick human body, a minimal X-ray (100 keV) skin dose rate of 6.94 μGy_{air} s^{-1} was derived, which corresponds to a DAP rate of ~2.5 Gy_{air} cm^2 h^{-1} in interventional cardiology with X-rays continuously on. There is a large variation of DAP rate reported in the literature, from 38 Gy_{air} cm^2 h^{-1} to 324 Gy_{air} cm^2 h^{-1} in fluoroscopy procedures. Therefore, this DAP rate by perovskite detectors is at least an order of magnitude better than that offered by state-of-the-art commercial medical radiographic systems[41–46].

In conclusion, we prepared the Si-integrated $MAPbBr_3$ single crystal device using a low-temperature solution-processed molecular bonding method with the assistance of brominated APTES molecules. The insertion of this layer resulted in a significant reduction in dark current at higher bias, which is critical for the Si-integrated $MAPbBr_3$ single crystal detectors to sense a very low X-ray (8 keV) dose rate of <0.1 μGy_{air} s^{-1} with a high sensitivity of 2.1×10^4 μC Gy_{air}^{-1} cm^{-2}. We also showed that the X-ray dose to patients using the developed linear detector array can be dramatically reduced by 15–120-fold. These performances are several orders of magnitude better than the state-of-the-art commercial α-Se X-ray detectors, paving the way for the commercialization of perovskite X-ray detectors for medical and security check applications. The simple method reported here is low in cost, scalable, and enables the integration of X-ray detectors with Si readout circuits. In addition, this method provides a facile way to integrate $MAPbBr_3$ single crystals onto various generally used substrates at low temperatures in solution, which opens a new avenue for the application of perovskite materials in much broader fields, such as active-matrix flat-panel imagers and flat-panel displays.

Methods

Methods and any associated references are available in the online version of the paper.

Received 7 November 2016; accepted 2 March 2017;
published online 17 April 2017

References

1. Barber, H. B. *et al.* Semiconductor pixel detectors for gamma-ray imaging in nuclear medicine. *Nucl. Instrum. Methods Phys. Res. A* **395,** 421–428 (1997).
2. Kasap, S. *et al.* Amorphous and polycrystalline photoconductors for direct conversion flat panel X-ray image sensors. *Sensors* **11,** 5112–5157 (2011).
3. Parker, S. I., Kenney, C. J. & Segal, J. 3D—A proposed new architecture for solid-state radiation detectors. *Nucl. Instrum. Methods Phys. Res. A* **395,** 328–343 (1997).
4. Luke, P. N., Rossington, C. S. & Wesela, M. F. Low energy X-ray response of Ge detectors with amorphous Ge entrance contacts. *IEEE Trans. Nucl. Sci.* **41,** 1074–1079 (1994).
5. Szeles, C. CdZnTe and CdTe materials for X-ray and gamma ray radiation detector applications. *Phys. Status Solidi B* **241,** 783–790 (2004).
6. Jeong, M., Jo, W. J., Kim, H. S. & Ha, J. H. Radiation hardness characteristics of Si-PIN radiation detectors. *Nucl. Instrum. Methods Phys. Res. A* **784,** 119–123 (2015).
7. Stoumpos, C. C. *et al.* Crystal growth of the perovskite semiconductor $CsPbBr_3$: a new material for high-energy radiation detection. *Cryst. Growth Des.* **13,** 2722–2727 (2013).
8. Zhao, W. & Rowlands, J. A. X-ray imaging using amorphous selenium: feasibility of a flat panel self-scanned detector for digital radiology. *Med. Phys.* **22,** 1595–1604 (1995).
9. Dong, Q. *et al.* Electron-hole diffusion lengths >175 μm in solution-grown $CH_3NH_3PbI_3$ single crystals. *Science* **347,** 967–970 (2015).
10. Hu, M. *et al.* Distinct exciton dissociation behavior of organolead trihalide perovskite and excitonic semiconductors studied in the same system. *Small* **11,** 2164–2169 (2015).
11. Huang, J., Shao, Y. & Dong, Q. Organometal trihalide perovskite single crystals: a next wave of materials for 25% efficiency photovoltaics and applications beyond? *J. Phys. Chem. Lett.* **6,** 3218–3227 (2015).
12. Jeon, N. J. *et al.* Compositional engineering of perovskite materials for high-performance solar cells. *Nature* **517,** 476–480 (2015).
13. Lin, Q. *et al.* Electro-optics of perovskite solar cells. *Nat. Photon.* **9,** 106–112 (2014).
14. Liu, M., Johnston, M. B. & Snaith, H. J. Efficient planar heterojunction perovskite solar cells by vapour deposition. *Nature* **501,** 395–398 (2013).
15. Saidaminov, M. I. *et al.* High-quality bulk hybrid perovskite single crystals within minutes by inverse temperature crystallization. *Nat. Commun.* **6,** 7586 (2015).
16. Shi, D. *et al.* Low trap-state density and long carrier diffusion in organolead trihalide perovskite single crystals. *Science* **347,** 519–522 (2015).
17. Yang, Y. *et al.* Low surface recombination velocity in solution-grown $CH_3NH_3PbBr_3$ perovskite single crystal. *Nat. Commun.* **6,** 7961 (2015).
18. Zhou, H. *et al.* Interface engineering of highly efficient perovskite solar cells. *Science* **345,** 542–546 (2014).
19. Fang, Y. *et al.* Highly narrowband perovskite single-crystal photodetectors enabled by surface-charge recombination. *Nat. Photon.* **9,** 679–686 (2015).
20. Chen, Q. *et al.* Under the spotlight: the organic–inorganic hybrid halide perovskite for optoelectronic applications. *Nano Today* **10,** 355–396 (2015).
21. Wei, H. *et al.* Sensitive X-ray detectors made of methylammonium lead tribromide perovskite single crystals. *Nat. Photon.* **10,** 333–339 (2016).
22. Yakunin, S. *et al.* Detection of X-ray photons by solution-processed lead halide perovskites. *Nat. Photon.* **9,** 444–449 (2015).
23. Yakunin, S. *et al.* Detection of gamma photons using solution-grown single crystals of hybrid lead halide perovskites. *Nat. Photon.* **10,** 585–589 (2016).
24. Wang, G. *et al.* Wafer-scale growth of large arrays of perovskite microplate crystals for functional electronics and optoelectronics. *Sci. Adv.* **1,** e1500613 (2015).
25. Dou, L. *et al.* Atomically thin two-dimensional organic–inorganic hybrid perovskites. *Science* **349,** 1518–1521 (2015).
26. Miyazaki, N., Kuroda, Y. & Sakaguchi, M. Dislocation density analyses of GaAs bulk single crystal during growth process (effects of crystal anisotropy). *J. Cryst. Growth* **218,** 221–231 (2000).
27. Moram, M. A. *et al.* Young's modulus, Poisson's ratio, and residual stress and strain in (111)-oriented scandium nitride thin films on silicon. *J. Appl. Phys.* **100,** 023514 (2006).
28. Wang, J., Huang, Q.-A. & Yu, H. Size and temperature dependence of Young's modulus of a silicon nano-plate. *J. Phys. D* **41,** 165406 (2008).
29. Hopcroft, M. A., Nix, W. D. & Kenny, T. W. What is the Young's modulus of silicon? *J. Microelectromech. Syst.* **19,** 229–238 (2010).
30. Lim, P. H., Park, S., Ishikawa, Y. & Wada, K. Enhanced direct bandgap emission in germanium by micromechanical strain engineering. *Opt. Express* **17,** 16358–16365 (2009).
31. Wright, A. F. Elastic properties of zinc-blende and wurtzite AlN, GaN, and InN. *J. Appl. Phys.* **82,** 2833–2839 (1997).
32. Ning, Z. *et al.* Quantum-dot-in-perovskite solids. *Nature* **523,** 324–328 (2015).
33. Androulakis, J. *et al.* Dimensional reduction: a design tool for new radiation detection materials. *Adv. Mater.* **23,** 4163–4167 (2011).
34. Hecht, K. *Zum Mechanismus des lichtelektrischen Primärstromes in isolierenden Kristallen. Z. Phys.* **77,** 235–245 (1932).
35. Yin, W.-J., Shi, T. & Yan, Y. Unusual defect physics in $CH_3NH_3PbI_3$ perovskite solar cell absorber. *Appl. Phys. Lett.* **104,** 063903 (2014).
36. Kasap, S. O. X-ray sensitivity of photoconductors: application to stabilized a-Se. *J. Phys. D* **33,** 2853–2865 (2000).
37. Currie, L. A. Limits for qualitative detection and quantitative determination. application to radiochemistry. *Anal. Chem.* **40,** 586–593 (1968).
38. Büchele, P. *et al.* X-ray imaging with scintillator-sensitized hybrid organic photodetectors. *Nat. Photon.* **9,** 843–848 (2015).
39. Akinlade, B. I., Farai, I. P., Okunade, A. A. Survey of dose area product received by patients undergoing common radiological examinations in four centers in Nigeria. *J. Appl. Clin. Med. Phys.* **13,** 188–196 (2012).
40. Kirac, S. F. E. (ed.) *Advances in the Diagnosis of Coronary Atherosclerosis* (InTech, 2011).
41. Davies, A. G. *et al.* Do flat detector cardiac X-ray systems convey advantages over image-intensifier-based systems? Study comparing X-ray dose and image quality. *Eur. Radiol.* **17,** 1787–1794 (2007).
42. Viggiano, A. *et al.* Exposure reduction by optimization of the imaging toolchain in pulmonary vein isolation. *Eur. Heart J.* **34**(Suppl 1), P2344 (2013).
43. Ector, J. *et al.* Obesity is a major determinant of radiation dose in patients undergoing pulmonary vein isolation for atrial fibrillation. *J. Am. Coll. Cardiol.* **50,** 234–242 (2007).
44. Nof, E. *et al.* Reducing radiation exposure in the electrophysiology laboratory: it is more than just fluoroscopy times! *Pacing. Clin. Electrophysiol.* **38,** 136–145 (2015).
45. Davies, A. G. *et al.* X-ray dose reduction in fluoroscopically guided electrophysiology procedures. *Pacing. Clin. Electrophysiol.* **29,** 262–271 (2006).
46. Pantos, I., Patatoukas, G., Katritsis, D. G. & Efstathopoulos, E. Patient radiation doses in interventional cardiology procedures. *Curr. Cardiol. Rev.* **5,** 1–11 (2009).

Acknowledgements

This X-ray detector development and characterization work was financially supported by the Defense Threat Reduction Agency under award no. HDTRA1-14-1-0030. The KPFM study was supported financially by the National Science Foundation under awards DMR-1505535 and DMR-1420645. The authors thank S. Banerjee and D. Haden for discussions regarding X-ray dose rate calibration, and S. Valloppilly for his assistance in using the X-ray source in the XRD system (Rigaku Multiflex) for X-ray imaging.

Author contributions

J.H. conceived and supervised the project. W.W. synthesized materials and fabricated the devices. Y.Z. and W.W. conducted the X-ray imaging measurements. H.W. measured the photodetector performance. Q.X. and L.C. measured the device performance under 50 keV X-ray radiation. Y.F. performed the photoluminescence lifetime measurement. T.L. and A.G. performed the KPFM measurement. Y.D. conducted SEM and XRD experiments. Q.W. carried out the TEM measurement. All authors analysed the data. J.H. wrote the manuscript and all authors reviewed the manuscript.

Additional information

Supplementary information is available in the online version of the paper. Reprints and permissions information is available online at www.nature.com/reprints. Publisher's note: Springer Nature remains neutral with regard to jurisdictional claims in published maps and institutional affiliations. Correspondence and requests for materials should be addressed to J.H.

Competing financial interests

The authors declare no competing financial interests.

Methods

Materials. The materials used were methylamine bromine (MABr; synthesized in the laboratory in accordance with previous work[21]), lead bromide ($PbBr_2$; >98%, Sigma-Aldrich), hydrobromic acid (HBr; 48% wt/wt aq. soln, Alfa Aesar), (3-aminopropyl)triethoxysilane (APTES; >99%, Sigma-Aldrich), *N*,*N*-dimethylformamide (DMF; >99.8%, Alfa Aesar), 1,2-dichlorobenzene (DCB; >99%, Sigma-Aldrich), 2-propanol (IPA; >99.5%, Sigma-Aldrich), C_{60}; >99.5%, Nano-C) and BCP (>96%, Sigma-Aldrich).

Preparation of NH_3Br-terminated molecule-functionalized Si substrate. The sandpaper-polished and precleaned Si (p-type) wafer was placed into a mixture of DCB and APTES solvent (20:1) for 12 h at 50 °C and ultrasonically rinsed with IPA to obtain NH_2-terminated molecules on the surface. The wafer was then treated with HBr (aq.) to convert the amino groups into $-NH_3Br$ groups.

Growth of Si-integrated $MAPbBr_3$ single crystal. $PbBr_2$ (2.31 g) and 0.67 g MABr (molar ratio of $PbBr_2$ to MABr of 1.05) were dissolved in 6 ml DMF to form a clear solution and then filtered into a 50 ml beaker. A small droplet of the solution was dropped onto a glass coverslip by bringing the pipette tip into contact with the coverslip. The slip was then placed on top of the beaker with the droplet side face down. After the DMF solvent had evaporated at room temperature, the $MAPbBr_3$ single crystal seed (dimensions of ~300 μm) was generated on the coverslip. The NH_3Br-terminated molecule-functionalized Si wafer was then placed in the beaker, and the prepared seed was placed onto the wafer. The solution was heated to 70 °C and maintained this temperature for 6–8 h for the growth of the single crystal. The thin $MAPbBr_3$ single crystal was fabricated either in the same way as above, except that the crystal growth time was reduced to 5–15 min, or simply by using the method for the growth of the $MAPbBr_3$ single crystal seed but replacing the coverslip with modified Si wafer.

Device fabrication. The electron-transporting layers (20 nm C_{60} and 8 nm BCP) and semi-transparent cathode (25 nm Au) were sequentially deposited on the top surface of the $MAPbBr_3$ single crystal by thermal evaporation.

X-ray imaging. All X-ray imaging experiments were conducted on a home-made imaging system housed in the chamber of a Rigaku Multiflex Diffractometer. The diffractometer excites X-rays with a peak energy of 8 keV by impinging high-energy electrons onto a copper target. The dose rate of the outcoming X-ray was measured by an ion chamber dose sensor (Radcal Accu-Pro 10X6-1800). For X-ray imaging, the Si-integrated detector was aligned with the X-ray beam, modulated by a metallic optical chopper at a frequency of 35 Hz. For single-pixel imaging, the object, fixed on an x–y scanning stage (PI Q-545.240), was allowed to move in and out of the beam in both x and y directions to obtain a complete image. For linear-pixel array imaging, the object was scanned only in the y direction to obtain the object image. For signal acquisition of single-pixel detectors, the detector was biased at −1 to −7 V with a Keithley source-meter 2400, and the detector current was recorded by a lock-in amplifier (SRS SR830). The signal acquisition for multiple-pixel detectors was the same as that for the single-pixel detectors, except that a switching system (Keithley 7001/7158) was used to switch the common measurement circuit between different pixels.

Data availability. The data that support the plots within this Article and other findings of this study are available from the corresponding author upon reasonable request.